

# On the coupled geomorphological and ecohydrological organization of river basins

Kelly K. Caylor<sup>a,\*</sup>, Salvatore Manfreda<sup>a,b</sup>, Ignacio Rodriguez-Iturbe<sup>a</sup>

<sup>a</sup> Department of Civil and Environmental Engineering, Engineering Quadrangle, Princeton University, Princeton, NJ 08540, USA

<sup>b</sup> Dipartimento di Ingegneria e Fisica dell'Ambiente, Università degli Studi della Basilicata, Potenza I-85100, Italy

Received 17 March 2004; received in revised form 27 August 2004; accepted 27 August 2004

## Abstract

This paper examines the linkage between the drainage network and the patterns of soil water balance components determined by the organization of vegetation, soils and climate in a semiarid river basin. Research during the last 10 years has conclusively shown an increasing degree of organization and unifying principles behind the structure of the drainage network and the three-dimensional geometry of river basins. This cohesion exists despite the infinite variety of shapes and forms one observes in natural watersheds. What has been relatively unexplored in a quantitative and general manner is the question of whether or not the interaction of vegetation, soils, and climate also display a similar set of unifying characteristics among the very different patterns they presents in river basins. A recently formulated framework for the water balance at the daily level links the observed patterns of basin organization to the soil moisture dynamics. Using available geospatial data, we assign soil, climate, and vegetation properties across the basin and analyze the probabilistic characteristics of steady-state soil moisture distribution. We investigate the presence of organization through the analysis of the spatial patterns of the steady-state soil moisture distribution, as well as in the distribution of observed vegetation patterns, simulated vegetation dynamic water stress and hydrological fluxes such as transpiration. Here we show that the drainage network acts as a template for the organization of both vegetation and hydrological patterns, which exhibit self-affine characteristics in their distribution across the river basin. Our analyses suggest the existence of a balance between the large-scale determinants of vegetation pattern reflecting optimality in the response to water stress and the random small-scale patterns that arise from local factors and ecological legacies such as those caused by dispersal, disturbance, and founder effects.

© 2004 Elsevier Ltd. All rights reserved.

**Keywords:** Soil moisture dynamics; Plant water stress; River network; Geomorphology; Ecohydrology; Semi-arid; Vegetation patterns

## 1. Introduction

Recent years have seen dramatic advances in the quantitative description of the geomorphologic structure of river basins [26]. The interconnected system of hillslopes and the channel network possesses a profound order that manifests itself in a number of probabilistic

features whose basic characteristics remain unchanged regardless of scale, geology, or climate [18]. Despite the deep symmetry of structural organization in geomorphologic properties, the convergence of the biological and geophysical study of river basins is a remaining frontier in hydrological science. In particular, there exists a need to understand the interrelationship among biological, geophysical and geochemical approaches to the study of the earth system. In this regard, soil moisture is a crucial link between hydrological and biogeophysical processes through its controlling influence on transpiration, runoff generation, carbon assimilation and nutrient absorption by plants. Therefore, efforts to

\* Corresponding author. Tel.: +1 949 824 4327; fax: +1 949 824 3672.

E-mail addresses: [kcaylor@princeton.edu](mailto:kcaylor@princeton.edu) (K.K. Caylor), [manfreda@cima.unige.it](mailto:manfreda@cima.unige.it) (S. Manfreda), [irodrigu@princeton.edu](mailto:irodrigu@princeton.edu) (I. Rodriguez-Iturbe).

integrate the biological and geophysical aspects of river basins will require a focus on the interactive manner by which patterns of climate, vegetation and geomorphology are coupled in landscape patterns and dynamics [27].

The belief that ecological processes are evident in vegetation patterns has often been used to investigate the relationships between the spatial structure of vegetation and the nature of competition, disturbance, and resource heterogeneity across a range of ecosystems. Even still, many outstanding issues in plant ecology are directly related to an incomplete understanding of the dynamics and persistence of spatial patterns [17]. These include (1) the relationship between competition/facilitation, spatial pattern, and the persistence of biodiversity; (2) the relative importance of biotic and abiotic factors in structuring vegetation communities; (3) the role of both current and former plant patterns in determining the spatial distribution of resource availability; and (4) the time and space scales over which various disturbances affect spatial patterns and the consequences of spatial disturbances on long-term stability of vegetation communities.

Understanding how vegetation patterns arise within landscapes organized around river networks is a central challenge that integrates each of the four issues listed above [4]. There is a growing awareness of the important role that geomorphology exerts on vegetation structural dynamics and the generation of landscape-scale vegetation patterns in many semiarid landscapes [8,12]. Here we focus on the manner by which drainage networks act as a template for the organization of ecohydrological interactions that determine vegetation patterns within landscapes. In this regard, we view our effort as an attempt to integrate more fully the concept of self-organization observed to be present within many patterns of vegetation [23,31] with the scale-invariance and self-organized complexity known to exist in the geomorphological organization of river basins [33,34]. To this end, we link observed patterns in vegetation organization with the hydrological dynamics operating within the basin. The principles of such organization have important consequences regarding the impact of land cover change on hydrological dynamics in river basins, as well as the geomorphological evolution of landscapes under varying climate and vegetation regimes.

Given the deep coherence in geomorphological structure across different basins and strong interactions among climate, soils, and vegetation in determining hydrological dynamics, we propose that a geospatial framework applied to the network structure will reveal congruence among the geomorphic, hydrologic and vegetation patterns, even where the distributions of these basin characteristics are seemingly independent. In particular, it is our hypothesis that the various distributions of climate, vegetation and soils will lead to an emergent

organization in the spatial distribution of soil moisture, evapotranspiration and vegetation water stress within the basin. In order to address our research hypotheses, we develop a geomorphological framework of analysis that uses the channel network as a template around which the possible organization of vegetation, soils and the components of the hydrologic balance takes place. We then proceed to couple the patterns of vegetation, soil and climate to the hydrological dynamics within the basin by applying a previously developed model of the steady-state seasonal soil moisture dynamics. We investigate the resulting patterns of soil moisture, transpiration and simulated plant water stress derived from the soil moisture model in order to discern the presence of a coupled geomorphological and ecohydrological organization within these quantities.

## 2. The Rio Salado river basin

Because our present approach focuses on water-controlled ecosystems, where soil moisture is a critical controlling resource, we will attempt this goal through the study of a semiarid river network, the Upper Rio Salado basin in New Mexico (Fig. 1a). The upper portion of the Rio Salado basin is located near the Sevilleta Long-term Ecological Research (LTER) site in central New Mexico. The basin exists within and adjacent to the Cibola National Forest, and pronounced heterogeneity in vegetation composition along with significant topographic variation make it suitable for the type of analysis we

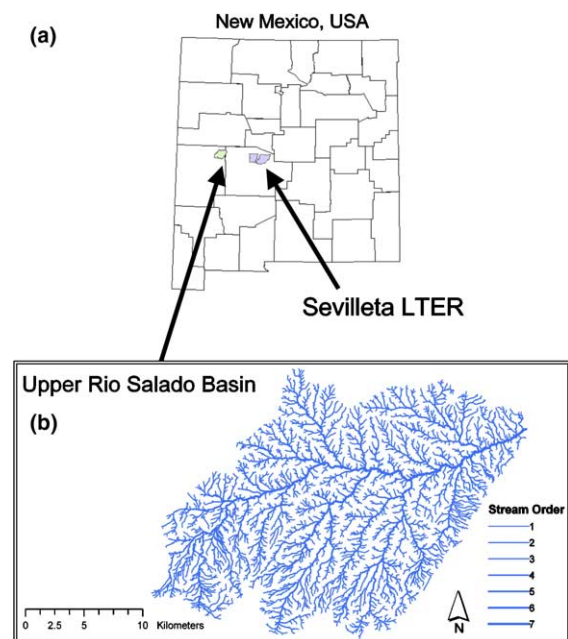


Fig. 1. Location of the Upper Rio Salado basin near Sevilleta LTER in New Mexico, USA (a). The lower panel (b) depicts the overall basin river network.

Table 1

Soil parameters associated with each of the three soil textures present within the Rio Salado Basin

Soil type	$\Psi_h$ (MPa)	$b$	$n$	$\bar{\Psi}_{s(\text{LOG})}$ (MPa)	$K_s$ (cm/d)	$s_h$	$s_{fc}$
Silt loam	−10.0	5.30	0.485	$-5.55 \times 10^{-3}$	62.2	.24	.69
Loam	−10.0	5.39	0.451	$-1.43 \times 10^{-3}$	60.0	.19	.54
Sandy loam	−10.0	4.90	0.435	$-7.04 \times 10^{-4}$	158.4	.14	.44

Notes: Soil parameters taken from Clapp and Hornberger [7]. All soils are assumed to have evaporation rates at plant wilting point of 0.10 cm/day.

are undertaking. The basin covers an area of 464 km<sup>2</sup>, and its elevation ranges from 1985 m above sea level (a.s.l.) to 2880 m a.s.l. We derive the stream network (Fig. 1b) from 30-m resolution USGS digital elevation models available from the seamless data distribution system (<http://seamless.usgs.gov>).

We use the USDA STATSGO soil database [35] to determine the pattern of soil texture within the Rio Salado basin (Fig. 3a). The basin contains three different soil textures—loam, sandy loam, and silty loam. In the upper part of the basin, loam and silty loam are most common, while the lower portion of the basin contains more sandy loam, particularly along the channel network. We relate soil texture to specific values of saturated hydraulic conductivity  $K_s$ , porosity  $n$ , field capacity  $\bar{\Psi}_s$ , and the hygroscopic point  $\Psi_h$  (Table 1) according to relationships defined in Clapp and Hornberger [7].

The distribution of vegetation composition (Fig. 3b) is taken from the USGS 28.5 m National Land Cover Dataset (NLCD) based on Landsat imagery [36], which we resample at 30-m resolution using a nearest neighbor technique. The composition of vegetation cover is represented by different plant functional types, which vary in their structure and use of water. The land cover is comprised of grassland (25.4%), shrubland (28%), and forest (45.7% of the total basin area), with a small fraction (<1%) of the basin classified as bare soil. In the Rio Salado area, forests are composed of open or moderately closed woodlands of pinyon pine (*Pinus edulis*) and stands of one-seed Juniper (*Juniperus monosperma*). Shrublands within the Rio Salado basin are dominated by the evergreen creosote bush (*Larrea tridentata*), which is a widespread and characteristic evergreen shrub of the Chihuahuan and Sonoran deserts. The most common species within the grasslands are galleta (*Hilaria jamesii*), and blue gramma (*Bouteloua gracilis*).

### 3. Geomorphological organization

In order to investigate the organization of hydrological dynamics resulting from the various distributions of climate, soils and vegetation within the Rio Salado basin, it is necessary to define an underlying geomorphological framework of analysis that links the network

structure to the patterns of each of these various quantities. In this study, the basin organization is represented using the geomorphological area function  $W(x)$ , which is a well described indicator of the fractal morphology contained within river networks [19,24]. The geomorphological area function is related to the width function, which measures the number of stream links at a given distance from the outlet measured through the network. The area function is found by dividing the basin into elementary areas and determining the distance of each area from the outlet as measured through the network flow path. In this way, the area function maps the two-dimensional structure of the basin into a one-dimensional support. Thus, at each distance, the value of  $W(x)$  is determined according to

$$W(x) = \frac{\sum_x A_x}{\sum_{x=0}^1 A_x \cdot \Delta x}, \quad (1)$$

where  $A_x$  denotes those elementary areas that are located at the same distance  $x$  from the outlet and  $\sum_{x=0}^1 A_x$  is the total sum of  $A_x$  for all  $x$  (i.e. the total area of the basin). Here  $x$  is measured through the stream network in constant intervals of  $\Delta x$  and takes values of  $0 < x \leq 1$  through normalization by the maximum upstream distance from the outlet. The resulting function may be interpreted as the probability distribution of area within the basin, such that

$$\sum_{x=0}^1 W(x) \Delta x = 1. \quad (2)$$

The geomorphological area function for the Rio Salado basin is provided in Fig. 2.

We characterize the statistical structure of  $W(x)$  through its spectral density function, denoted by  $S_W(f)$ . Marani et al. [19] show that  $S_W(f)$  exhibits power-law scaling for many basins of different geomorphological characteristics, such that  $S_W(f) \propto f^{-\beta}$ , with the value of  $\beta$  found to vary between 1.7 and 1.9. Functions that exhibit this behavior are self-affine, and belong to the general class of processes known as fractional Brownian motion. The presence of self-affinity implies statistical scale invariance, so that the process remains statistically unchanged when proper scaling factors are applied to each axis, e.g., distance from the outlet and area distribution. Therefore, for the self-affine geomorphological area function  $W(x)$ , we can state that

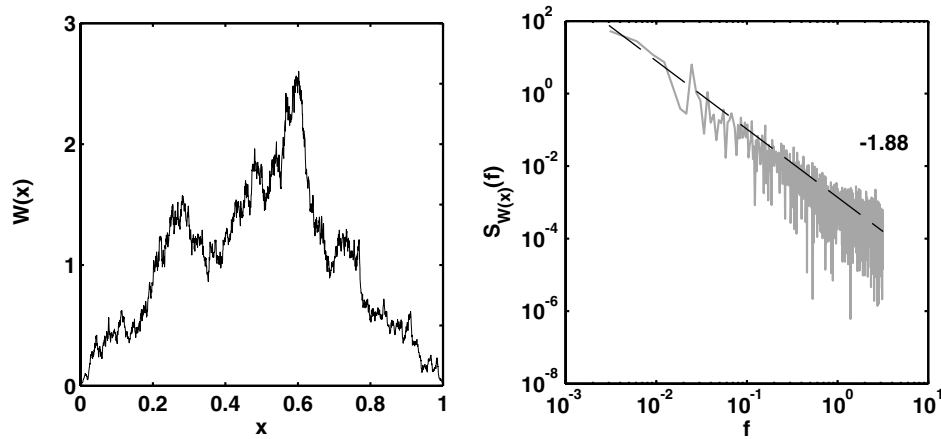


Fig. 2. Normalized area function for the Upper Rio Salado basin, and its corresponding power spectra density (radians<sup>-1</sup>).

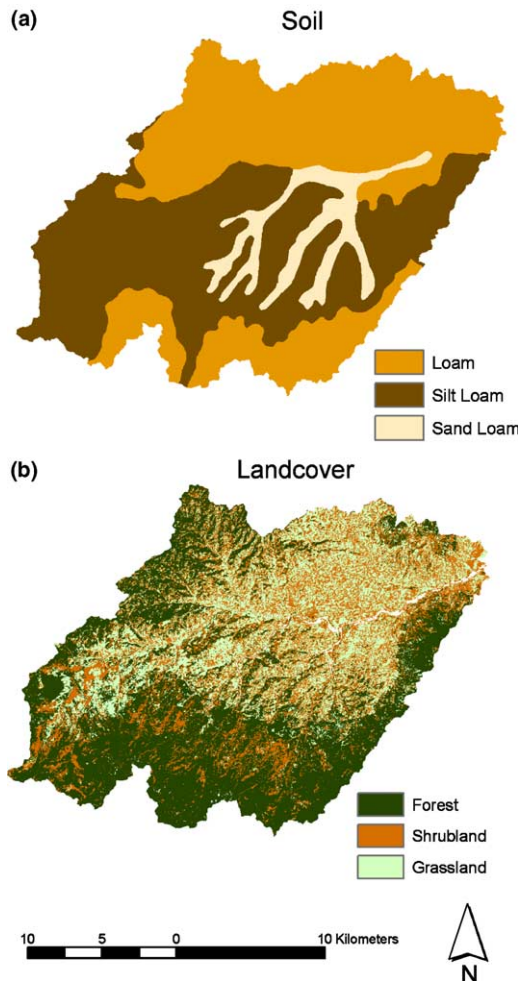


Fig. 3. Spatial patterns of the soil (a) and vegetation (b) distributions within the Rio Salado basin.

$$W(x + \gamma\Delta x) - W(x) \stackrel{d}{=} \gamma^H [W(x + \Delta x) - W(x)], \quad (3)$$

where  $d$  means equality in the statistical sense,  $H$  is the Hurst exponent, which is related to  $\beta$  according to

$H = (\beta - 1)/2$ ,  $\gamma$  is an arbitrary rescaling factor along the distance axis, and  $\gamma^H$  is the self-affine scaling factor along the area distribution axis. The values of  $H$  and  $\beta$  indicate the persistence of a function, such that when  $H > 1/2$  and  $\beta > 2$  we say that the fractional Brownian motion exhibits persistence, and when  $H < 1/2$  and  $\beta < 2$  the process is said to display antipersistence. Ordinary Brownian motion is a special case of fractional Brownian motion that occurs when  $H = 1/2$  and  $\beta = 2$ . The power spectra  $S_W(f)$  for  $W(x)$  within both basin one and basin two are presented in Fig. 2, for which power law spectra and self-affinity are clearly shown. The area function for the Rio Salado basin displays the scaling relationship  $S_W(f) \propto f^{-\beta}$  with a value of  $\beta$  equal to 1.88. Having established the self-affine organization of the basin network through the analysis of the geomorphological area function, we now focus on the distribution of soils and vegetation within the Rio Salado basin.

We analyze the patterns of vegetation and soil distribution within the Rio Salado basin using the area function concept defined above. For any arbitrary quantity  $j$  distributed within the basin, we define the function  $W_j(x)$ , which is analogous to the area function presented above and describes the distribution of the quantity  $j$  at a distance  $x$  measured through the network

$$W_j(x) = \frac{\sum_x j_x}{\sum_{x=0}^1 j_x \cdot \Delta x}. \quad (4)$$

Through this definition of  $W_j(x)$  we use the land cover data to determine the vegetation area function for the various land cover components (tree, shrub, and grass). In the case of the vegetation area function, the number of elementary areas containing a given land cover type at each distance is divided by the total number of elementary areas containing the assigned land cover type. The resulting vegetation area functions for trees, shrubs and grasses ( $W_{\text{Tree}}(x)$ ,  $W_{\text{Shrub}}(x)$ , and  $W_{\text{Grass}}(x)$ )

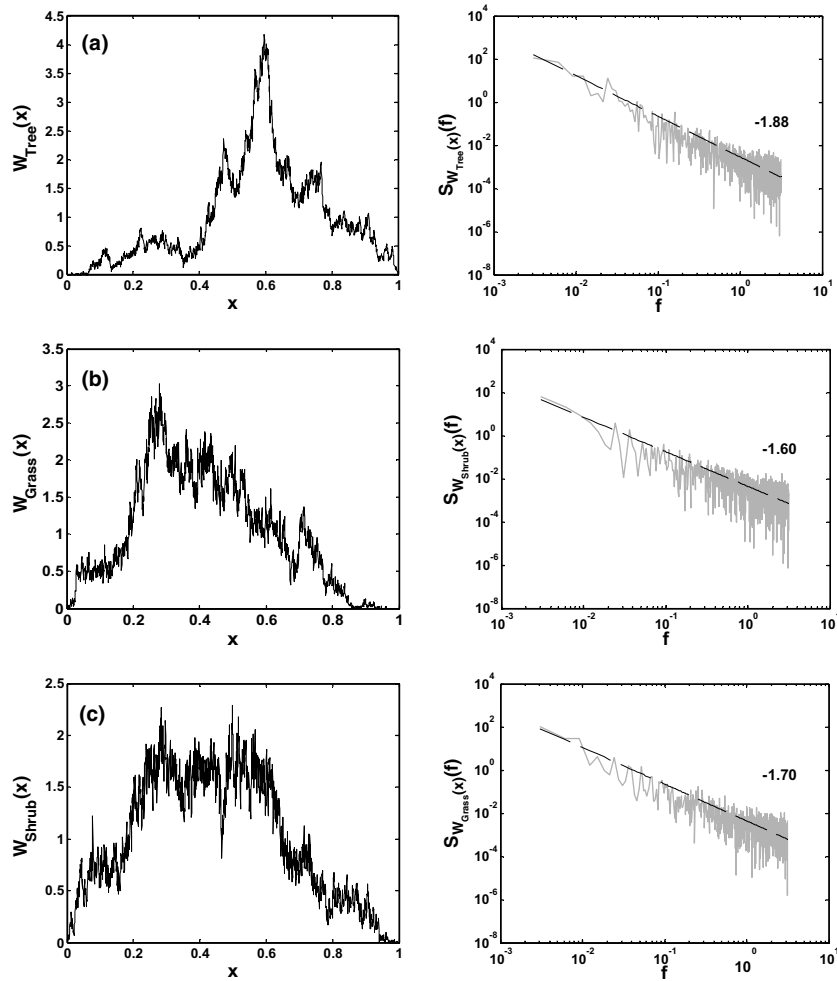


Fig. 4. Normalized vegetation area functions and their power spectra density functions for each of the three vegetation types—trees (a), shrubs (b) and grasses (c) in the Upper Rio Salado.

respectively) are given for the Upper Rio Salado basin in Fig. 4. Although these vegetation area functions exhibit markedly different characteristics for each of the land cover types, comparisons among the total basin and subbasins within the upper Rio Salado demonstrates consistency in these differences. As in the case of the geomorphological area function, the power spectra of the vegetation area functions exhibit clear power law scaling (Fig. 4). The spectra of shrub and grass vegetation distribution have smaller slopes than the spectra of area distribution, indicating an enrichment of high frequency variation, and therefore greater small-scale spatial variability in the distribution of these types of vegetation compared to the distribution of tree vegetation (cf. Fig. 3).

#### 4. Soil moisture and water balance

We derive the steady-state probability distribution of soil moisture and the components of the steady-state

water balance using an analytical model of stochastic soil moisture balance first proposed by Rodriguez-Iturbe et al. [27] and presented in Laio et al. [13]. The starting point of the model is the stochastic differential equation for the daily soil water balance, i.e.

$$nZ_r \frac{ds}{dt} = \varphi(s, t) - \chi(s), \quad (5)$$

where  $n$  is the porosity,  $Z_r$  is the active depth of soil,  $s$  is the degree of saturation or relative soil moisture content,  $\varphi(s, t)$  is the marked Poisson process of storm arrivals and moisture inputs into the soil, and  $\chi(s)$  is the rate of losses from the soil. The input function  $\varphi(s, t)$  is the portion of rainfall that infiltrates the soil, which is rainfall  $R(t)$  minus the sum of interception  $I(t)$  and saturation excess  $Q(s, t)$ . The loss function  $\chi(s)$  represents losses due to the sum of evapotranspiration  $E(s)$  and leakage  $L(s)$ . In this analysis, the subsurface flow and the interaction with the phreatic surface are neglected, so the cells of the basin are considered as independent and not interconnected. Such an assumption may be

justified for arid and semiarid conditions where the water table is sufficiently deep and subsurface flow is a minor component of the dynamics [22].

Because climate, vegetation, and soil properties vary across the basin, we must account for most of the substantive variation in hydrological variables to define accurately the local scale dynamics. The climate regime of the area is that of a typical semiarid environment, with a pronounced growing season that occurs during the northern hemisphere summer. Analysis of long-term meteorological records (Table 2) indicates that during the growing season (May–September) the Rio Salado basin receives a mean annual rainfall depth that varies according to elevation, ranging between 220 and 325 mm/yr. The analyses pertaining to the water balance presented here are restricted to the growing season only. The rate of rainfall,  $R(t)$ , is represented as a marked Poisson process of storm arrivals in time with rate  $\lambda$  ( $\text{day}^{-1}$ ), each storm having a depth  $h$  (mm), where  $h$  is modeled as an exponentially distributed random variable with mean  $\alpha$  (mm). Using 12 years of temperature and rain gauge data (1990–2001) recorded in the Sevilleta research area and the Rio Salado basin (Table 2), we develop relationships between elevation and each of the rainfall process parameters ( $\lambda$  and  $\alpha$ ). The resulting lin-

ear relationships between elevation  $x$  (in meters a.s.l.) and these two rainfall parameters are

$$\lambda = 8 \cdot 10^{-5}x + 0.1025; \quad R^2 = 0.84, \quad (6)$$

$$\alpha = 0.0014x + 2.56; \quad R^2 = 0.63. \quad (7)$$

The model incorporates canopy interception  $l(t)$  by assuming a threshold of rainfall depth  $d$ , below which no water effectively penetrates the canopy [27]. The storage capacity of vegetation varies between trees, shrubs, and grasses as described in Table 3. The frequency of infiltration events is given by

$$\lambda' = \lambda e^{-d/\alpha}. \quad (8)$$

Rainfall results in an infiltration depth into the soil, which is taken to be the minimum of effective storm depth,  $h$ , and  $nZ_r(1-s)$ . This formulation reflects the fact that only a fraction of  $h$  can infiltrate when the rainfall amount exceeds the storage capacity of the soil column, and rainfall in excess of soil capacity produces saturation runoff  $Q(s, t)$ .

The sum of the evapotranspiration function  $E(s)$  and leakage function  $L(s)$  results in the total loss function  $\chi(s)$ , which varies throughout the basin due to variation in soils, climate and vegetation. Assuming no interaction

Table 2

Rainfall stations considered to estimate the spatial variability of the rainfall pattern within the Rio Salado basin

Station	Period	Latitude	Longitude	Elevation	$T_{\text{avg}}$ ( $^{\circ}\text{C}$ )	$\alpha$ (mm)	$\lambda$ ( $\text{d}^{-1}$ )
40 (Sevilleta)	1990-01	34.36	-106.69	1600	22.4	4.62	0.23
41 (Sevilleta)	1990-01	34.22	-106.80	1538	22.8	5.13	0.22
42 (Sevilleta)	1990-01	34.37	-106.54	1971	20.6	5.94	0.27
43 (Sevilleta)	1990-01	34.40	-107.04	1766	22.4	5.10	0.23
44 (Sevilleta)	1990-01	34.30	-106.93	1503	23.7	4.44	0.23
45 (Sevilleta)	1990-01	34.41	-106.93	1547	23.1	4.49	0.20
Pietown (NOAA)	1990-01	34.33	-107.59	2426	17.2	5.70	0.28

Notes: Parameters are derived for the growing season only (May–September).

Table 3

Vegetation parameters associated with each land cover type

Land cover type	$Z_r$ (cm)	$d$ (cm)	$\Psi_w^a$ (MPa)	$\Psi^*$ (MPa)	Height <sup>b</sup> (m)	LAI <sup>c</sup> ( $\text{m}^2/\text{m}^2$ )	$\alpha_s^d$	$g_{s\text{MAX}}^e$ ( $\text{mmol}/\text{m}^2\text{s}$ )
Tree	150	0.20	-2.8	-0.50	4.0	1.50	0.10	150
Shrub	40	0.15	-5.0	-0.40	1.0	0.50	0.15	180
Grass	30	0.10	-4.0	-0.10	0.5	0.25	0.12	400

Notes: Rooting depth ( $Z_r$ ), canopy interception ( $d$ ), wilting point ( $\Psi_w$ ), and the soil potential at which plants begin to limit transpiration ( $\Psi^*$ ) are used within the steady-state soil moisture model. Vegetation height, leaf area index (LAI), shortwave albedo ( $\alpha_s$ ) and maximum stomatal conductance ( $g_{s\text{MAX}}$ ) are used to calculate potential maximum evapotranspiration ( $E_{\text{max}}$ ) using a Penman–Monteith formulation.

<sup>a</sup> Tree data from Williams and Ehleringer [39]. Shrub and grass data from E. Small, personal communication.

<sup>b</sup> Sevilleta LTER Vegetation Map Data [29].

<sup>c</sup> Shrub and grass data from Yang and Milne [41]. Tree data inferred from MODIS 8-day, 1-km LAI/IPAR product (MOD15A2 v.4), acquired on August 5, 2001. Documentation for the MOD15A2 product is available at <http://edcdaac.usgs.gov/modis/mod15a2.html>, Sevilleta subset file used (MOD15A2.A2001217.cs\_sevillet.004.2003135091339.hdf) is available at: <ftp://edcsgs16.cr.usgs.gov/orders/eosval/2001/sevillet/MODIS/MOD15A2/>

<sup>d</sup> Shortwave albedo values of shrub and grass taken from Small and Kurk [30], tree albedo inferred from values for typical coniferous vegetation in Bonan [2].

<sup>e</sup> Tree data from Williams and Ehleringer [39], shrub data from Yan et al. [40], grass data from Larcher [15].

with the underlying soil layers and water table,  $L(s)$  represents vertical percolation with unit gradient

$$L(s) = \frac{K_s}{e^{\beta(1-s_{fc})} - 1} [e^{\beta(s-s_{fc})} - 1], \quad (9)$$

where  $K_s$  is the vertical saturated hydraulic conductivity,  $s_{fc}$  is the field capacity, and  $\beta = 2b + 4$  when  $b$  is the pore size distribution index [13]. The value of  $s_{fc}$  is related to a corresponding soil matric potential (Table 1) through empirical soil–water retention curves [7]. The stochastic soil moisture model incorporates losses due to evaporation from the soil as well as transpiration from the plant. At the daily time scale, evapotranspiration  $E(s)$  spans three regimes (Fig. 5). The first regime corresponds to the soil evaporation regime and defines  $E(s)$  as linearly increasing with  $s$ , from 0 at the hygroscopic point  $s_h$ , to the maximum rate of soil evaporation  $E_w$  at the wilting point  $s_w$ . Here we assume  $E_w$  to be 1 mm/day. The second regime is the stressed evapotranspiration regime, which has a linear rise in  $E(s)$  from  $E_w$  at  $s_w$ , to  $E_{max}$  at  $s^*$ , where  $s^*$  is the soil moisture level at which the plant begins to close stomata in response to water stress. As with  $s_{fc}$ , the values of  $s_h$ ,  $s_w$ , and  $s^*$  are related to corresponding matric potentials  $\Psi_h$ ,  $\Psi_{s_w}$ , and  $\Psi_{s^*}$ . (Tables 1 and 3) according to soil–water retention curves derived from the presentation of Clapp and Hornberger [7].

The third regime of evapotranspiration is the unstressed evapotranspiration regime, during which plant water use is decoupled from soil moisture status and total evapotranspiration remains constant at  $E_{max}$ , which represents the average daily rate under well-watered conditions. For soil moisture values above  $s_{fc}$  leakage takes place according to Eq. (9). The value of  $E_{max}$  depends on many factors, the most critical of which are plant physiology, canopy structure, and the prevailing climatic conditions during the growing season. For this reason, we use a Penman–Montieth equation to estimate

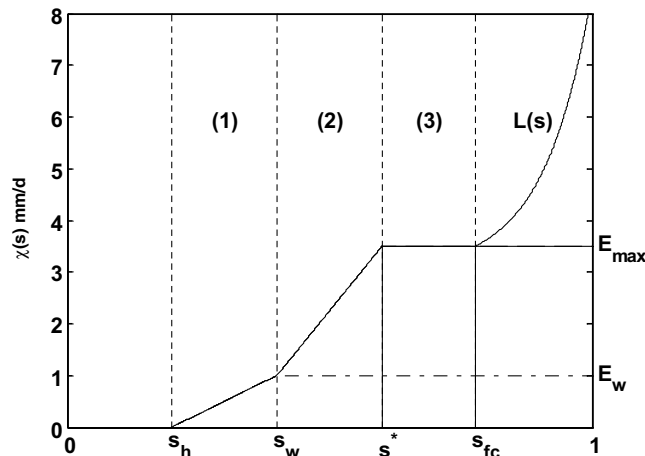


Fig. 5. Daily loss function due to the three regimes of evapotranspiration  $E(s)$  as well as leakage  $L(s)e$ .

maximum the evapotranspiration rate when soil moisture is not limiting plant transpiration. The Penman–Monteith equation predicts latent heat flux according to

$$\lambda E = \frac{\Delta R_n + \rho C_p g_a \cdot \delta e}{\Delta + \gamma(1 + g_a/g_c)}, \quad (10)$$

where  $E$  is the transpiration rate ( $\text{kgm}^{-2}\text{s}^{-1}$ ),  $\lambda$  is the latent heat of vaporization ( $\text{Jkg}^{-1}$ ),  $\Delta$  is the slope of the curve relating saturation vapor pressure to temperature ( $\text{Pa}^\circ\text{C}^{-1}$ ),  $R_n$  is the net radiation of the plant canopy ( $\text{Jm}^{-2}\text{s}^{-1}$ ),  $\rho$  is the density of air ( $\text{kgm}^{-3}$ ),  $C_p$  is the specific heat capacity of air ( $\text{J}^\circ\text{C}^{-1}$ ),  $g_a$  is the aerodynamic conductance of the vegetation canopy ( $\text{ms}^{-1}$ ),  $\delta e$  is the vapor pressure deficit (Pa),  $\gamma$  is the psychrometric constant ( $\text{Pa}^\circ\text{C}^{-1}$ ), and  $g_c$  is the vegetation canopy conductance ( $\text{ms}^{-1}$ ). Meteorological data from Station 45 in the Sevilleta LTER (Table 2) are used to determine characteristic values of daytime average incoming shortwave radiation  $SW_{INC}$  ( $\text{Jm}^{-2}\text{s}^{-1}$ ), mean air temperature  $T_{avg}$  ( $^\circ\text{C}$ ), and mean vapor pressure  $e$  (Pa) during the growing season. Although we assume a constant average daily  $SW_{INC}$  during the growing season across the basin, meteorological data from nearby stations indicate that a gradient in mean growing season temperature is present across the Rio Salado basin, with average temperature decreasing according to basin elevation. Thus, we define the following linear relationship between elevation (in meters a.s.l.) and mean growing season daily air temperature  $T_a$  ( $^\circ\text{C}$ ) based on meteorological observations (Table 2)

$$T_a = -0.0068x + 33.34; \quad R^2 = 0.92. \quad (11)$$

Using the value of  $T_a$  at each elevation determined according to Eq. (11) and the mean vapor pressure taken from Station 45, we determine the saturation vapor pressure  $e_s$  and the vapor pressure gradient  $\delta e$  at each location in Rio Salado basin. The net radiation  $R_n$  is calculated based on the presentation in Jones [11]. In this formulation of net radiation, the temperature of the vegetation canopy and the atmosphere are assumed to be equal ( $T_{leaf} = T_a$ ) so that the expression for net radiation reduces to

$$R_n = \alpha_s SW_{INC} + \sigma T_s^4 - \sigma(T_a + 273.15)^4, \quad (12)$$

where  $\alpha_s$  is the fraction of shortwave radiation absorbed by the canopy for each vegetation type (dimensionless, Table 3),  $\sigma$  is the Stefan–Boltzmann constant ( $5.67 \times 10^{-8} \text{Wm}^{-2}\text{K}^{-4}$ ) and  $T_s$  is the apparent radiative temperature of the atmosphere (K) determined using the empirical relationship in Friend [10] as

$$T_s = T_a + 273.15 - 0.825 \exp(3.54 \times 10^{-3} \cdot SW_{INC}). \quad (13)$$

The product of the vegetation maximum stomatal conductance ( $g_{sMAX}$ , Table 3) and leaf area index

(LAI, Table 3) determines the total canopy conductance under well-watered conditions

$$g_c = g_{s\text{MAX}} \cdot \text{LAI}. \quad (14)$$

A field study of *Larrea tridentata* [40] provides the maximum stomatal conductance of shrub vegetation, while the maximum stomatal conductance of pinyon–juniper woodlands is from the presentation of Williams and Ehleringer [39]. A characteristic value of desert grassland vegetation taken from Larcher [15] specifies the grass maximum stomatal conductance. In order to calculate total canopy conductance, we assume that the leaf area of grasses and shrubs are constant, equal to 0.25, and 0.50 respectively. These values are within the range of observed leaf area for shrubs and grasses in the Sevilleta LTER [41]. We infer the leaf area of tree vegetation using a remotely sensed image of LAI acquired by the MODIS sensor at 1 km resolution (MOD15A2, 8-day, 1-km LAI/FPAR product, see notes to Table 3). Within the MODIS image, the average LAI of 1-km pixels underlain by forest is approximately 1.5, and we use this value for all land cover pixels that contain tree vegetation.

The aerodynamic conductance ( $g_a$ ) term in the Penman–Monteith equation is a function of vegetation height ( $h_v$  [m], Table 3) and wind speed according to

$$g_a = \frac{k^2 u_z}{(\ln[(h-d)/z_0])^2}, \quad (15)$$

where  $k$  is the dimensionless von Karman constant (0.41),  $u_z$  is the average daily wind speed (from meteorological records in Table 2) at the reference height  $h$  (taken to be 2 m above the canopy height reported in Table

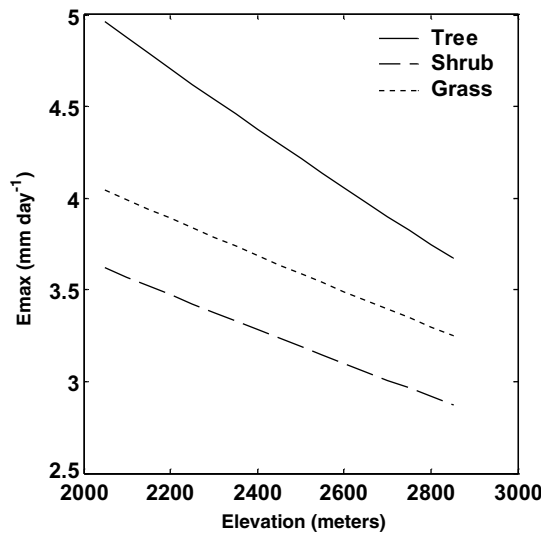


Fig. 6. Effect of elevation and vegetation type on the simulated maximum evapotranspiration rate ( $E_{\text{max}}$ ) within the Upper Rio Salado basin.

3),  $d$  is the displacement height equal to  $0.64h_v$  and  $z_0$  is the roughness length equal to  $0.13h_v$  [6]. The average daily value of  $E_{\text{max}}$  ( $\text{mm d}^{-1}$ ) is determined by scaling the value of  $E_{\text{max}}$  ( $\text{mm s}^{-1}$ ) from Eq. (10) by the average day length during the growing season. Fig. 6 summarizes the resulting patterns of  $E_{\text{max}}$  for each of the three vegetation types across the elevation gradient present within the Rio Salado basin. The elevation gradient in mean daily air temperature described by Eq. (11) drives changes in  $E_{\text{max}}$ , due to lower net radiation and decreased vapor pressure gradients at higher elevations. Differences in  $E_{\text{max}}$  between vegetation types at a given elevation are primarily due to differences in maximum stomatal conductance and canopy leaf area according to Eq. (14).

## 5. Mean and variance of soil moisture

The steady-state solution for the mean soil moisture,  $\langle s \rangle$  and the variance in soil moisture,  $\sigma^2(s)$ , are derived from steady-state relative soil moisture probability distribution function given in [13] as

$$p(s) = \begin{cases} \frac{C}{\eta_w} \left( \frac{s-s_h}{s_w-s_h} \right)^{\frac{\lambda'(s_w-s_h)}{\eta_w}} e^{-\gamma s}, & s_h < s \leq s_w, \\ \frac{C}{\eta_w} \left[ 1 + \left( \frac{\eta}{\eta_w} - 1 \right) \left( \frac{s-s_w}{s^*-s_w} \right) \right]^{\frac{\lambda'(s^*-s_w)}{\eta-\eta_w}} e^{-\gamma s}, & s_w < s \leq s^*, \\ \frac{C}{\eta} e^{-\gamma s + \frac{\lambda'}{\eta}(s-s^*)} \left( \frac{\eta}{\eta_w} \right)^{\frac{\lambda'(s^*-s_w)}{\eta-\eta_w}}, & s^* < s \leq s_{fc}, \\ \frac{C}{\eta} e^{-(\beta+\gamma)s + \beta s_{fc}} \left( \frac{\eta e^{\beta s}}{(\eta-m)e^{\beta s_{fc}} + m e^{\beta s}} \right)^{\frac{\lambda'}{\beta(\eta-m)} + 1} \\ \times \left( \frac{\eta}{\eta_w} \right)^{\frac{\lambda'(s^*-s_w)}{\eta-\eta_w}} e^{\frac{\lambda'}{\eta}(s_{fc}-s^*)} & s_{fc} < s \leq 1, \end{cases} \quad (16)$$

where  $p(s)$  is the probability distribution of soil moisture, and

$$\eta_w = \frac{E_w}{nZ_r}, \quad (17)$$

$$\eta = \frac{E_{\text{max}}}{nZ_r}, \quad (18)$$

$$m = \frac{K_s}{nZ_r(e^{\beta(1-s_{fc})} - 1)}. \quad (19)$$

The varying control that soils and vegetation exert on the steady-state distribution of the growing season relative soil moisture is shown in Fig. 7. The distributions are shown for each of the three land cover types (tree, shrubs, and grasses) and three soil types (sandy loam, loam, and silty loam) using fixed values of leaf area index and climate (specified by  $T_a$ ,  $\alpha$ , and  $\lambda$ ). The steady-state mean value of relative soil moisture during the growing season is highest for silty loam and lowest for sandy loam regardless of the vegetation type. In con-

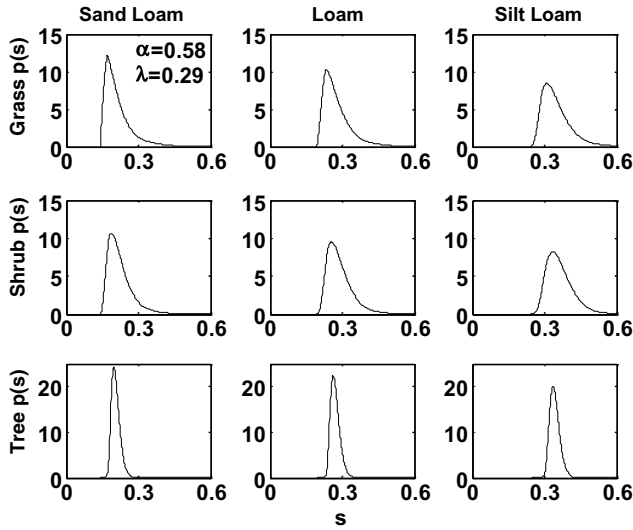


Fig. 7. Steady-state probability distribution functions for relative soil moisture during the growing season. Each of the nine vegetation-soil combinations present within the Upper Rio Salado basin is shown at the basin average elevation (~2400 m).

trast, the variance of relative soil moisture is highest for grass vegetation and lowest for trees, regardless of the soil texture. These patterns are affirmed in the spatial distribution of the mean and variance of steady-state distribution of relative soil moisture (Fig. 8a and b), which are seen to primarily respond to the distribution of soil and land cover respectively (Fig. 3a and b).

Over long time scales the mean inputs of moisture are in balance with the losses so that the steady-state water balance reduces to  $\langle \phi \rangle - \langle \chi \rangle = 0$ , or  $(\langle R \rangle - \langle I \rangle - \langle Q \rangle) - (\langle E \rangle + \langle L \rangle) = 0$ . Under these conditions, the mean rainfall intensity is derived [13] as

$$\langle R \rangle = \alpha \cdot \lambda, \quad (20)$$

and the expected rate of interception as

$$\langle I \rangle = \alpha \lambda (1 - e^{-d/\alpha}). \quad (21)$$

The mean runoff is determined according to

$$\langle Q \rangle = \alpha \left( \eta + \frac{K_s}{nZ_r} \right) p(1), \quad (22)$$

where  $p(1)$  is the probability distribution of soil moisture,  $p(s)$ , evaluated at saturation. The expression for evapotranspiration can be written as the sum of  $E_s$ , which is evapotranspiration under stressed conditions ( $s_h < s < s^*$ ) and  $E_{ns}$ , which occurs during unstressed conditions ( $s^* \leq s < 1$ ). The expected values of these quantities are given by

$$\langle E \rangle = \langle E_s \rangle + \langle E_{ns} \rangle, \quad (23)$$

$$\langle E_s \rangle = \alpha \lambda e^{-d/\alpha} p(s^*) - \alpha \eta p(s^*), \quad (24)$$

$$\langle E_{ns} \rangle = E_{\max} [1 - P(s^*)], \quad (25)$$

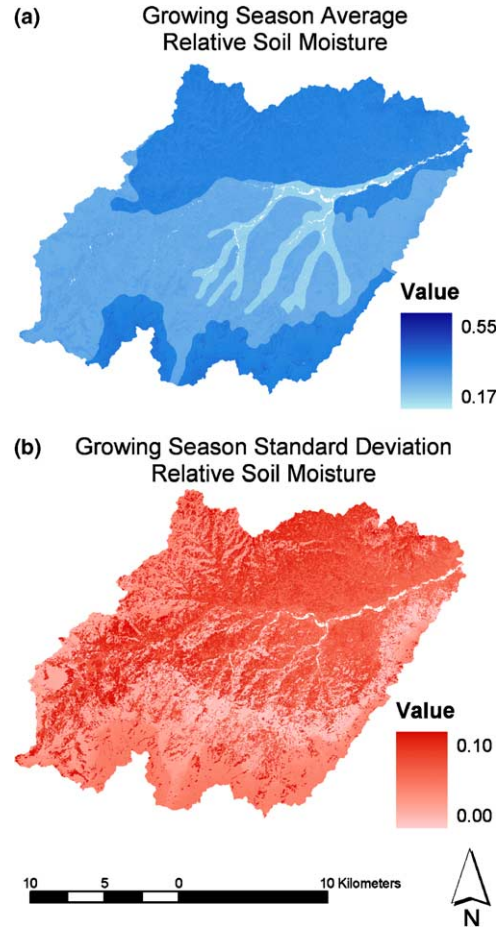


Fig. 8. Spatial patterns of the standard deviation (a) and mean (b) of the steady-state relative soil moisture during the growing season.

where  $P(s^*)$  and  $p(s^*)$  are the cumulative probability and the probability distribution function of  $s$  evaluated at  $s = s^*$ , respectively. Equations for the solution of  $P(s)$  are provided in [13], and  $p(s)$  is given in Eq. (16). The application of Eqs. (20)–(25) for each individual pixel in the basin provides the spatial distribution of the expected values of the various water balance terms.

We group the various loss terms into two distinct components:  $\chi_a$ , which represents seasonal average losses via the atmosphere ( $\langle E \rangle + \langle I \rangle$ ); and  $\chi_s$ , which represents seasonal average losses through the ground ( $\langle L \rangle + \langle Q \rangle$ ). The area function analogy presented above for the distribution of vegetation allows for the expression of these losses as the functions  $W_{\chi_a}(x)$  and  $W_{\chi_s}(x)$  (Fig. 9). In the case of atmospheric losses  $\chi_a$  (Fig. 9a) the function very closely resembles the overall area function itself. In contrast, the distribution of soil losses  $\chi_s$  (Fig. 9b) resembles the distribution of the grasses and shrubs within the basin, which generate the great majority of the soil losses within the Rio Salado because of their shallower rooting depths. The power spectra of the two loss functions,  $W_{\chi_a}(x)$  and  $W_{\chi_s}(x)$ , display clear power law character (Fig. 9c and d).

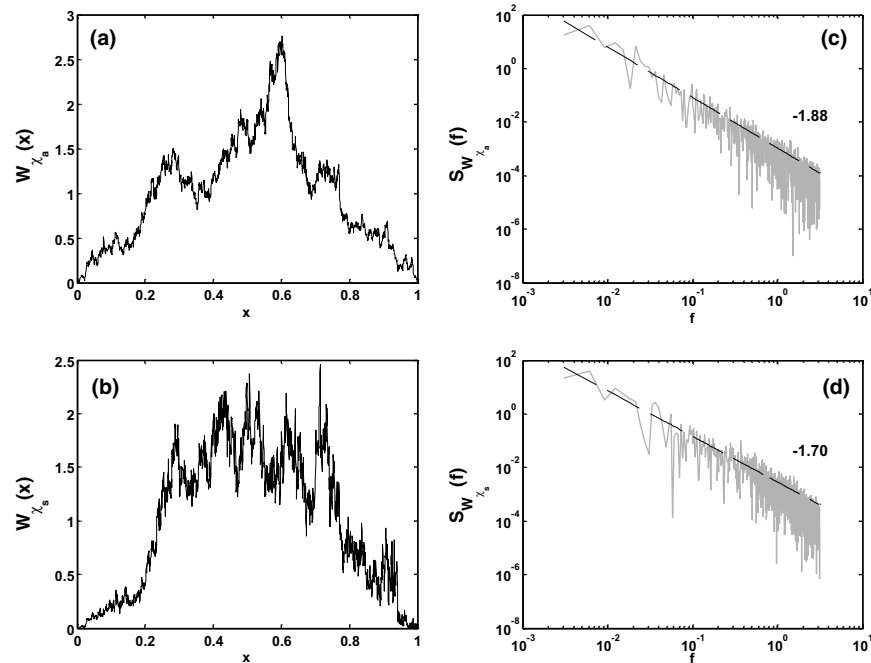


Fig. 9. Area functions of the atmospheric ( $\gamma_a$ ) and soil ( $\gamma_s$ ) loss functions and their corresponding spectral density functions for the Upper Rio Salado basin.

## 6. Soil moisture organization within the basin

We now investigate the spatial pattern of the steady-state mean relative soil moisture presented in Fig. 8a. With the objective of linking relative soil moisture patterns with the geomorphological organization present in river basins, we introduce the soil moisture profile of the basin,  $\langle s \rangle(x)$ . This function describes the changing values of mean relative soil moisture throughout the basin, and is defined as the average value of the steady-state mean relative soil moisture of all the points located at the same distance  $x$  from the basin outlet measured through the network. Thus

$$\langle s \rangle(x) = \frac{\sum_{i=1}^{N_x} \langle s \rangle_i}{N_x}, \quad (26)$$

where  $N_x$  is the number of elementary pixels at distance  $x$  measured through the drainage network, and  $\langle s \rangle_i$  is mean value of the steady-state probability distribution of relative soil moisture at each of these  $N_x$  locations. As in the use of the geomorphological area function, these functions collapse the two-dimensional spatial structure of the soil moisture into a one-dimensional function that describes its variability through the basin network. The loss of information regarding soil moisture pattern due to the degradation of the two-dimensional field into a single linear transect is balanced by the coherence of associating the soil moisture pattern to the structure of the drainage network. The soil moisture profile and corresponding power spectrum that result from this analysis as applied to the basin are reported in Fig. 10. The power-law spectral density

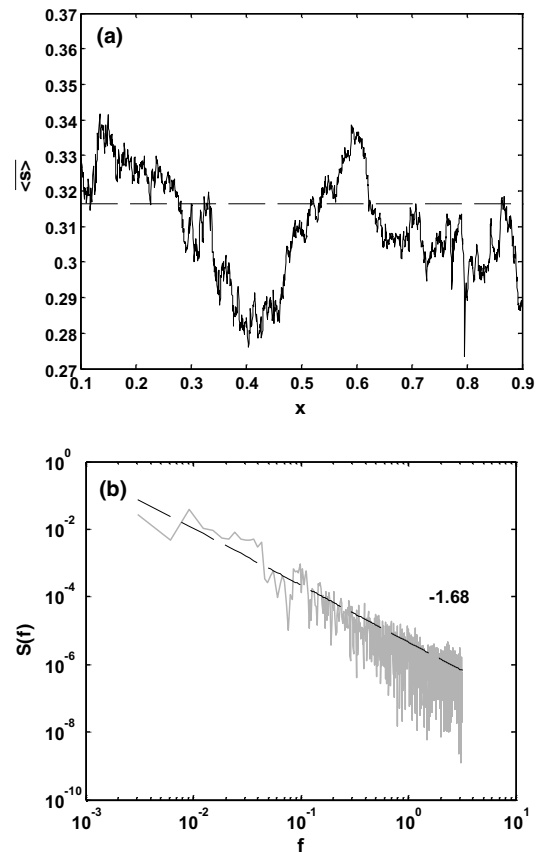


Fig. 10. Soil moisture profile  $\langle s \rangle$  and associated power spectra for the Upper Rio Salado basin.

function (Fig. 10b) indicates that  $\overline{\langle s \rangle}(x)$  is a self-affine process despite the extended two-dimensional patterns of mean soil moisture imposed by our coarse specification of soil texture (Fig. 3a).

## 7. Dynamic water stress

The effect of soil moisture deficit on plant water stress links the dynamics of plant response to the action of climate and soil. In this section, we consider the argument that water stress of plants plays a fundamental role in the organization of the vegetation pattern. In order to assess the vegetation stress patterns within the Rio Salado basin, we consider the dynamic water stress relationship presented in Porporato et al. [21]. Here we provide a brief summary of the concepts used to formulate a dynamic water stress index based on the probabilistic structure of soil moisture. We define the normalized degree of stress experienced by vegetation under a given level of soil moisture content as the “static” water stress,  $\zeta$ , given in [21] as

$$\zeta(t) = \begin{cases} 1 & \text{if } s(t) \leq s_w, \\ \left[ \frac{s^* - s(t)}{s^* - s_w} \right]^q & \text{if } s_w \leq s(t) \leq s^*, \\ 0 & \text{if } s(t) > s^*, \end{cases} \quad (27)$$

where the exponent  $q$  accounts for the non-linear relationship between the plant stress and the soil water content and the quantities  $s^*$  and  $s_w$  are defined in the previous section.

The daily static water stress does not account for the seasonal distribution of the frequency and duration of stress periods below a certain threshold  $\xi$ , which we define as  $n_\xi$  and  $T_\xi$  respectively [21]. Given the expression of the steady-state probability distribution of relative soil moisture,  $p(s)$ , presented above and in [13], the average number of excursions of below the soil moisture level  $\xi$  during the duration of a single growing season,  $T_{\text{seas}}$ , is  $\bar{n}_\xi = T_{\text{seas}} v(\xi)$ , where  $v(\xi) = \chi(\xi)p(\xi)$  and  $\chi(\xi)$  represents the loss function evaluated at  $\xi$  [21]. The mean duration of an excursion below the threshold  $\xi$  is given as

$$\bar{T}_\xi(\xi) = \frac{P(\xi)}{\chi(\xi)p(\xi)}. \quad (28)$$

Because the value of stress is greater than zero only during those periods when the relative soil moisture is below the value of  $s^*$ , the values of  $\bar{T}_{s^*}$  and  $\bar{n}_{s^*}$  provide a means of characterizing the portion of the growing season during which stress conditions exist. Accordingly, these additional terms are used to define the average dynamic water stress during a growing season  $\bar{\theta}$ , given in [21] as

$$\bar{\theta} = \begin{cases} \left( \frac{\bar{\zeta}' \bar{T}_{s^*}}{k T_{\text{seas}}} \right)^{1/\sqrt{\bar{n}_{s^*}}} & \text{if } \bar{\zeta}' \bar{T}_{s^*} < k T_{\text{seas}}, \\ 1 & \text{otherwise,} \end{cases} \quad (29)$$

where the term  $\bar{\zeta}'$  represents the average static water stress during periods of stress conditions, which we derive from the probability distribution function of soil moisture and the relationship between  $s$  and  $\zeta$  presented in Eq. (27). Here we define  $k$  as an index of plant resistance to water stress that can be interpreted as the average value of  $\bar{\zeta}'$  that a plant can experience without suffering permanent damages when the duration of stress is the entire growing season. The inverse of the square root of  $\bar{n}_{s^*}$  as an exponent in the formulation of the dynamic water stress allows for the non-linear effects of stress frequency on vegetation performance (cf. the discussion in [21]).

Because the values of  $k$  and  $T_{\text{seas}}$  serve to normalize the value of dynamic stress in Eq. (29), average dynamic water stress values are sensitive to both of these two parameters. Here we have attempted to assign varying  $k$  values that reflect the differences in life history and physiology for each of the three vegetation types present in the basin, while recognizing the difficulty in approximating the complex response of plants to water stress in such a manner. Considering the climatic characteristics and significant drought tolerance of the Rio Salado vegetation, we adopt values of the parameter  $k$  equal 0.7 for tree and shrub vegetation and 0.5 for grass vegetation. The steady-state probability distribution of relative soil moisture for tree vegetation (Fig. 7) is confined to a narrow range of values around the mean, which leads to persistently high stress levels predicted for the tree vegetation. Because the steady-state *pdf* of soil moisture for tree vegetation rarely exceeds the value of  $s^*$ , the mean duration of stress is essentially the entire length of the growing season. Therefore, despite the use of a relatively high  $k$  value for woody vegetation, we find that the predicted dynamic water stress for tree vegetation derived from the steady-state soil moisture distribution is greater than  $k$  throughout the basin. Under such conditions, the presence of tree vegetation within the Rio Salado basin is not consistent with the predictions of the steady-state soil moisture model.

The presence of tree vegetation within the Rio Salado basin is nevertheless consistent with the role of transient soil moisture dynamics associated with early spring snowmelt that occurs within the upper portions of the basin. Although data regarding annual snowfall in upper elevations of the Rio Salado are not available, meteorological records from surrounding areas suggests the high likelihood that the large amount of winter snowfall (primarily snow) that occurs at these locations greatly influences the initial soil moisture conditions at the start of the growing season. Studies investigating the annual water budget of woodlands in northern

New Mexico indicate that winter precipitation may account for up to 50% of the annual water inputs in these ecosystems [37], and that snowmelt processes can lead to near-saturated conditions during springtime snowmelt [3]. Based on data from weather stations proximate to the Rio Salado basin, the average winter snowfall increases from <13cm at 2000m (Magdalena, NM; NCDC COOP Station # 295353) to over 127cm at 2400m (Pietown, NM; NCDC COOP Station #296812), the altitude at which woodland vegetation begins to become more common.

The dynamic water stress described above assumes that the transient dynamic of soil moisture associated with the initial condition ( $s_0$ ) is not a significant factor in determining the overall seasonal dynamics of the temporal evolution of soil moisture. However, in the case that the initial condition of soil moisture is very high due to near-saturated conditions at the start of the growing season, it is necessary to determine the role of initial conditions in determining the overall stress conditions experienced by the vegetation during the subsequent growing season. For any initial condition  $s_0$  above the steady-state mean soil moisture  $\langle s \rangle$ , it is possible to determine the mean first passage time  $\bar{T}_{(s)}(s_0)$  (in days) of the stochastic process between  $s_0$  and  $\langle s \rangle$  [14], which we use to rescale the dynamic water stress experienced by the vegetation. This reformulation of the dynamic water stress represents the stress experienced by vegetation during the portion of the growing season not influenced by the transient dynamics associated with an initial condition when water is readily available. The determination of  $\bar{T}_{(s)}(s_0)$  follows the presentation of Laio et al. [14], and is given by

$$\bar{T}_{(s)}(s_0) = \bar{T}_{s_0}(s_0) - \bar{T}_{(s)}(\langle s \rangle) + \frac{1}{v(\langle s \rangle)} - \frac{1}{v(s_0)} + \gamma \int_{\langle s \rangle}^{s_0} (1/v(u) - \bar{T}_u(u)) du, \quad (30)$$

where  $\bar{T}_{(s)}(\langle s \rangle)$ ,  $\bar{T}_{s_0}(s_0)$ ,  $v(\langle s \rangle)$ , and  $v(s_0)$  are solved using the equations presented above,  $\gamma$  is the ratio of the active soil depth,  $nZr$ , to the mean rainfall depth  $\alpha$ , and the final term in Eq. (30) is found through numerical integration. In order to account for water storage at the beginning of the growing season, the mean first passage time  $\bar{T}_{(s)}(s_0)$  is used to scale the dynamic water stress  $\bar{\theta}$  according to the following relationship [28]:

$$\bar{\theta}' = \frac{T_{\text{seas}} - \bar{T}_{(s)}(s_0)}{T_{\text{seas}}} \bar{\theta}. \quad (31)$$

This simple modified dynamic water stress  $\bar{\theta}'$  allows for an effective synthesis of the interaction between plants, soils, and climate systems with important transient responses that occur at the start of the growing season. Based on the rapid increase in average winter snowfall observed between the Magdalena (2000m) and Pietown

(2400m) meteorological stations, we have assigned initial conditions of  $s_0 = s_{fc}$  in the portion of the Rio Salado basin that lies above 2350m. We examine the resulting effects of this initial condition on the modified dynamic water stress experienced by the vegetation within the basin.

Fig. 11 exhibits the differences in dynamic water stress experienced by each of the vegetation types for each soil type in the presence and absence of initially wet conditions. For the cases without initial conditions (Fig. 11a, c and e), the water stress of the tree vegetation is consistently at or near one, indicating the lack of suitability of the Rio Salado basin for tree vegetation when considering only the steady-state soil moisture distribution that arises from the growing season climate. We find that the inclusion of an initial condition such that the soil moisture at the beginning of the growing season is equal to field capacity at elevations above 2350m predicts a dramatic reduction in tree vegetation dynamic water stress at locations above 2350m (cf. Fig. 11a, c, e and b, d, f). In contrast, we observe little effect of

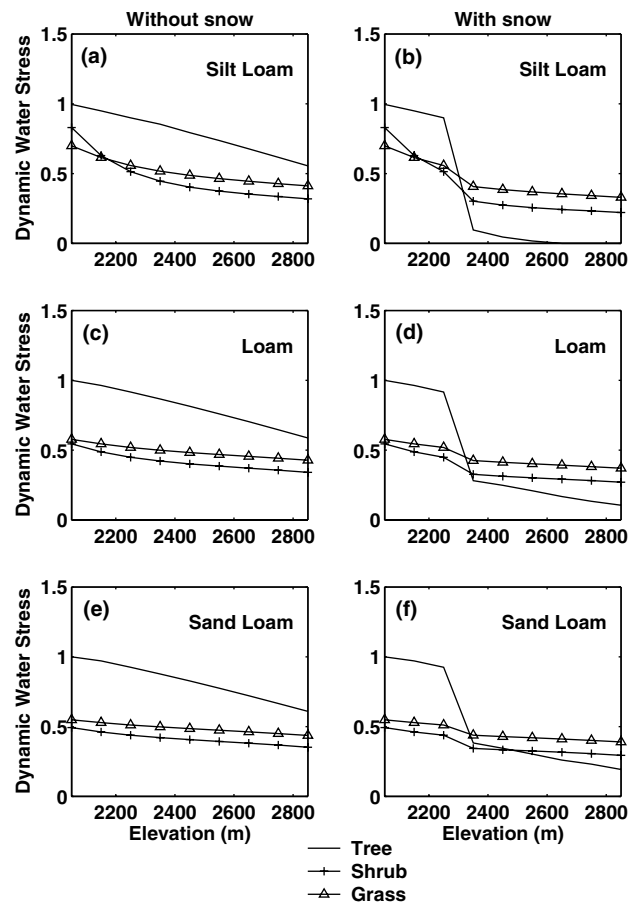


Fig. 11. Dynamic water stress (a, c, e) and modified dynamic water stress (b, d, f) for tree, shrub, and grass vegetation across the Rio Salado elevation gradient. The modified dynamic water stress is derived for each soil type based on an initial condition of  $s = s_{fc}$  at the start of the growing season.

initial conditions on the water stress experienced by shrub and grass vegetation. We find that the shallower rooting depth of shrub and grass vegetation (Table 3) reduces the effect of the snowmelt processes by limiting the amount of additional soil moisture available to these vegetation types at the start of the growing season. The reduction in water stress for woodland vegetation in the upper portion of the Rio Salado basin is in agreement with the general observation that significant winter snow accumulation and high soil moisture values during the subsequent spring snowmelt are common in semiarid pinyon–juniper woodlands [38]. Therefore, we suggest that both transient and steady-state soil moisture dynamics are important when contemplating the distribution of vegetation patterns within highly seasonal semiarid ecosystems. The modified dynamic water stress profile based on the consideration of winter snow accumulation is presented in Fig. 12. This modified profile represents the average  $\bar{\theta}'$  for all pixels located at the same distance from the outlet measured throughout

the network. As the distance from the outlet increases, the average modified dynamic water stress decreases. These results indicate the strong effect that the initial conditions have on the dynamic water stress, particularly in the tree vegetation, which can most effectively exploit the large store of soil moisture that exists at the start of the growing season due to spring snowmelt.

Given the importance of water stress in determining the distribution of vegetation within semiarid river basins, the derivation of a characteristic dynamic water stress profile may provide insight into the extent to which the current pattern of vegetation is self-organized around the landscape-scale variation in dynamic water stress. We investigate this organization through a comparison of the existing vegetation pattern to two alternative hypothetical vegetation distributions. The first is the distribution of vegetation that arises from a random assignment of vegetation type at each location within the basin, under the constraint that the proportions of overall land cover composition are preserved. The second hypothetical pattern is the one arising from the specification of the vegetation type that exhibits the lowest dynamic water stress at each location within the basin. From the sole point of view of water stress, we could say that the second pattern represents an optimal or ideal distribution of vegetation. Fig. 13 portrays the basin patterns resulting from each of these two alternative specifications of land cover, as well as the actual pattern observed within the Rio Salado basin. A visual comparison of these three patterns (actual, random, and ideal) suggests that the actual pattern of vegetation distribution contains elements of both the highly organized large-scale ideal pattern, as well as the characteristic small-scale variation associated with the random pattern. The modified dynamic stress profile based on each of the two hypothetical distributions (random and ideal), as well as the actual dynamic water stress profile are presented in Fig. 14. Our results suggest that the current vegetation pattern is configured such that it is well constrained by these two extremes of vegetation organization, so that the basin tends to experience an intermediate level of water stress that is neither random nor ideal. The existence of a distribution of water stress globally bounded by the random and ideal vegetation distribution may allow for the development of dynamic modeling approaches for predicting the distribution of vegetation pattern in river basins under conditions of changing climatic and edaphic regimes [5]. Moreover, it is likely that the vegetation patterns in water-controlled ecosystems tend to approach an optimal configuration in terms of water stress but are subject to important and decisive random contingencies of an altogether different character. Conceptually, this is not different from the notion of feasible optimality at work in the organization of the drainage network [26].

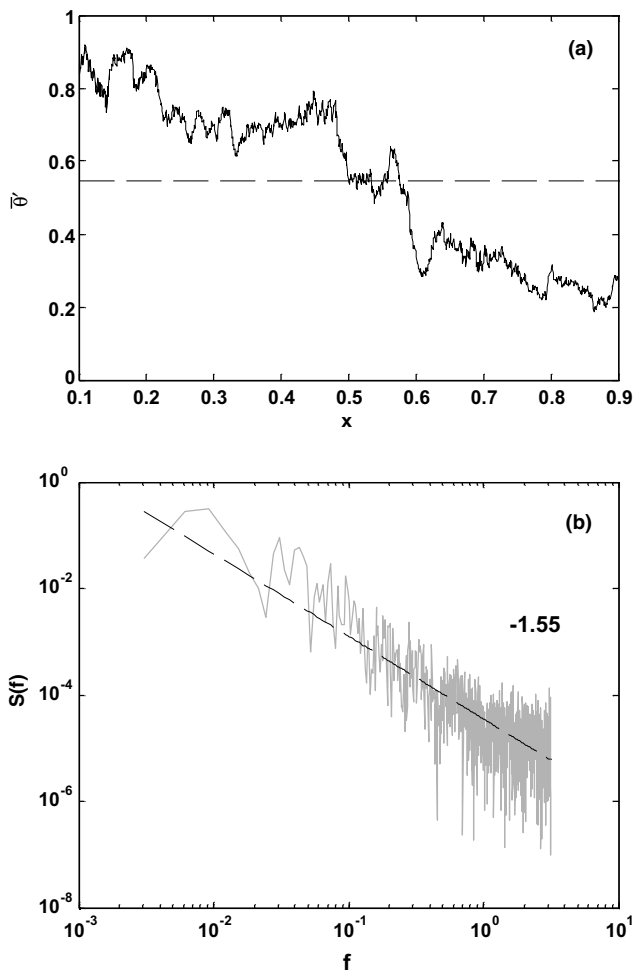


Fig. 12. Modified dynamic stress profile and associated power spectra for the Upper Rio Salado basin.

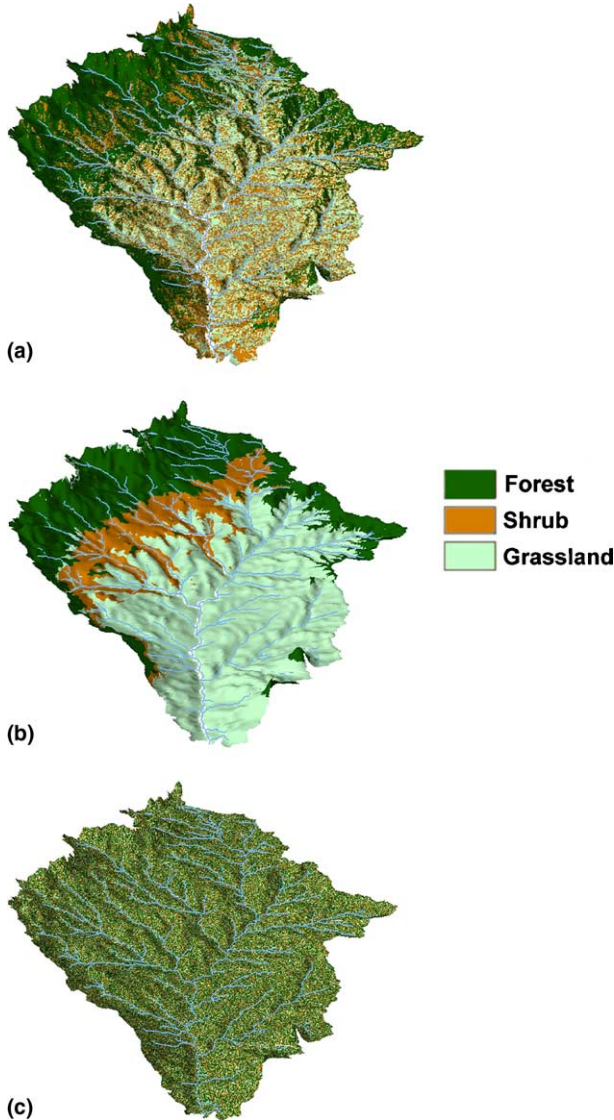


Fig. 13. Actual pattern of vegetation in the Rio Salado basin (a) compared to two hypothetical patterns. Panel (b) shows the pattern of vegetation type that corresponds to the minimum modified dynamic water stress at each location. Panel (c) depicts a vegetation pattern resulting from a random assignment of vegetation type that preserves the overall proportion of each type.

## 8. Geographical and topological descriptions of basin geomorphological structure

The framework of network organization presented here has focused on the area function as a key geomorphological representation of basin structure. This approach is geographic in nature, collapsing the structure of the river basin into a single linear measure of distance. Alternatively, we can consider the topological structure of the network, defined by the branching hierarchy of individual stream segments. The topological and geographical descriptions of basin structure do not contain equivalent information regarding the nature

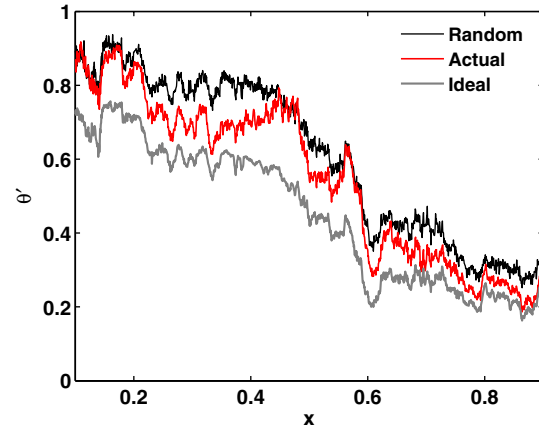


Fig. 14. Comparison of the actual modified dynamic stress profile (solid red line) to random (solid black line) and ideal (solid gray line) distributions of vegetation within the Rio Salado basin.

of vegetation, soil, and climate patterns within the basin. Therefore, when the organization of the basin is characterized through the topological structure of the network, patterns observed in the area function analogy are not observed. Indeed, the topological structure of the network tends to average out the effects of the characteristic elevation gradient that underlies the Rio Salado basin so that geomorphic gradients that are organized within the basin according to the distance from the outlet are no longer evident. Fig. 15 reveals the difference in pattern observed between geographical and topological expressions of network organization. Under the assumption that the distribution of  $j$ ,  $W_j(x)$ , is equivalent to the distribution of area,  $W(x)$ , then the ratio  $W_j(x)/W(x) = 1$  is true for all values of  $x$ . To assess the departure between the distribution of  $j$  and the distribution of areas within the drainage network, we define the quantity

$$\Delta_j(x) = \left( \frac{W_j(x)}{W(x)} \right) - 1 \quad (32)$$

with the expected value,  $\Delta_j(x) = 0$  for values of  $x$  when the assumption  $W_j(x)/W(x) = 1$  is met. Following Eq. (32) we determine  $\Delta_{z_a}(x)$ , which is the departure between the distribution of atmospheric losses,  $W_{z_a}(x)$ , and the distribution of areas,  $W(x)$ . The resulting distribution of the ratio between atmospheric losses and the area function increases steadily from the outlet (Fig. 15a). This trend mirrors the changing spatial distribution of rainfall parameters, which increase with elevation according to Eqs. (6) and (7). Therefore, in the case of a geographical gradient, we find that the normalized average atmospheric losses per unit area  $\Delta_{z_a}$  increases with distance from the outlet  $x$  as measured through the basin flow paths. However, when the properties of hydrological organization are investigated using the exceedance probability of total upstream evapotranspiration above any randomly chosen point in the network,

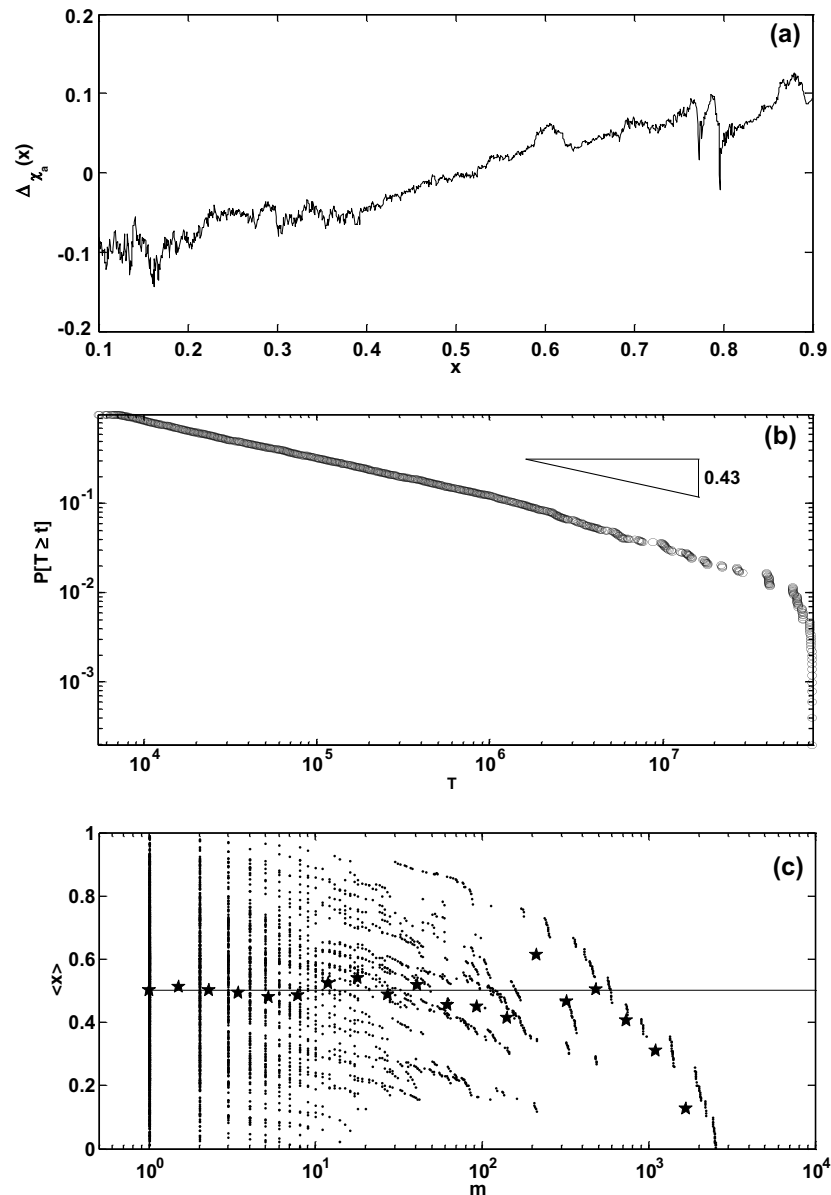


Fig. 15. Normalized atmospheric losses per unit area,  $\Delta x_a$ , increasing with distance from the outlet,  $x$ , measured through the network (a). Exceedance probability of total upstream evapotranspiration above a randomly chosen point in the drainage network,  $P[T > t]$ , (b). Normalized average distance from the outlet for links of different magnitudes (c).

$P[T > t]$ , we find that the Rio Salado basin (and all sub-basins therein) exhibits characteristic scaling properties that are consistent with known scaling properties of river networks. In particular, the exceedance probability of cumulative upstream evapotranspiration for any randomly chosen point in the basin is a power law with slope  $-0.43$  (Fig. 15b), which is very similar to the observed geomorphological scaling exponent in the distribution of contributing areas within river basins [26]. Thus, despite the presence of a geographic trend in atmospheric losses per unit area (Fig. 15a), there is no trend manifested within evapotranspiration per unit area when analyzed according to stream magnitude

(Fig. 15b), where magnitude is a surrogate of upstream contributing area. The reason for the above is that basin topology tends to smooth many geographical differences across the river basin. As an example, the average normalized distance from the outlet is approximately 0.5 for streams of almost all magnitudes (Fig. 15c), except for the very highest magnitude streams whose directly contributing areas are very close to the outlet. Therefore, the topological structure of river basins tends to preserve an average value of hydrological quantities within the network structure (here expressed as constant evapotranspiration per unit area) even in the presence of pronounced inhomogeneous geographical distributions

of such quantities within the basin. This observation is consistent with the assumption that spatially variant physical quantities such as directly contributing area or energy expenditure per unit area of streambed can be considered random variables with an expected value that is constant and independent of the magnitude of the link [25].

## 9. Conclusions

The present work attempts to unify approaches of investigating geomorphological and ecohydrological patterns through the development of a common geomorphological framework of analysis (here defined as the geomorphological area function). We find that the structure of the river network reverberates with that of the ecohydrological patterns, and we find that the statistical organization of the basin geomorphology as expressed in the area function is congruent with that of the soil moisture patterns. Both the area function  $W(x)$  and the soil moisture profile  $\overline{\langle s \rangle}(x)$  exhibit power law spectral density functions, a reflection of their clear self-affine character. These similarities occur despite the fact that the soil moisture profile is independent of the area distribution. This suggests a correspondence in the underlying processes that organize these two patterns. A large number of correlated physical variables underlie the structure of all drainage networks. We view the co-organization of vegetation, climate, and topography to be an emergent property of river basins, and suggest that such organization should manifest itself in all types of basins through patterns similar to those demonstrated here.

Recent studies regarding the spatial pattern of soil moisture within landscapes have revealed the pronounced fluctuations existing in both the mean and variance of soil moisture fields [20]. A particular focus of these studies has been the specification of locations within river basins that reflect generic spatio-temporal basin characteristics [32]. However, theoretical expectations regarding the covariance between soil moisture and hydrological fluxes have demonstrated that heterogeneous patterns of land surface and soil conditions can either enhance or erode spatial patterns of soil moisture depending on the soil moisture status of the landscape [1], raising some doubts about the existence of a ‘characteristic’ basin response. The results of this study further reveal the complexity arising from the coupled interactions of climate, soils, and vegetation on basin soil moisture and hydrological fluxes. Within the Rio Salado basin, estimated differences in the variance of the steady-state relative soil moisture probability distribution are caused mainly by the varying rooting depth of each vegetation type, despite the similarity in mean relative soil moisture value between different vegetation types

when they are located in similar soil structures (Fig. 7). In this case, the variation in rooting depth between trees, shrubs, and grasses appears to be a controlling factor in distribution of both the total soil water content and soil losses (i.e. leakage and runoff). However, across the Rio Salado basin, atmospheric losses do not exhibit a distribution that is characteristic of either the vegetation or the soil properties. Instead, we find that the variation in rainfall explains most of the variation in total evapotranspiration. The limited availability of soil moisture within the basin means that the different values of  $E_{\max}$  do not greatly influence atmospheric losses, which primarily consist of stressed evapotranspiration.

Our analyses suggest the existence of a balance between the large-scale determinants of vegetation pattern reflecting optimality in the response to water stress and the random small-scale patterns that arise from local factors and ecological legacies such as those caused by dispersal, disturbance, and founder effects. In the Rio Salado basin, we observe an organization that yields an actual pattern of vegetation distribution found to lie within the envelope described by the ideal vegetation pattern that corresponds to the minimization of water stress within the basin, and a random one that preserves the overall percentage of the different types of vegetation (Fig. 14). Although we present a hypothesis regarding the dynamic origin of such an organization elsewhere [5], we note that the structure of the river network itself may serve as a constraint on the suite of possible vegetation patterns, through its effect on the dispersal of vegetation along hillslopes and between subbasins.

The actions of geomorphology, climate, and vegetation each have an effect on the patterns of soil moisture distribution in semiarid landscapes. Here we have focused on the geomorphological organization of a basin that spans a climatic gradient driven by elevation. In this case, the gradient in elevation across the Rio Salado basin describes a shift in climate sufficient to delineate differences in the relative water stress of the common vegetation types within the basin. Therefore, because we have specifically neglected subsurface lateral flow, it is important to consider that our suggestion of a geomorphological constraint on vegetation pattern is distinct from any additional topographically based organization of vegetation pattern that may develop from the lateral and vertical redistribution of soil moisture across a hillslope or other elevation gradient [12]. However, the aridity of the Rio Salado basin means that very little moisture remains in the soil between rainfall events and we expect that in this case lateral redistribution is not likely to play a significant role on the dynamics of soil moisture [22].

Finally, the patterns described in this study have demonstrated a degree of co-organization between vegetation, climate, and topography despite the potential disparity in time (and space) scales over which vegeta-

tion communities and drainage basins evolve. In particular, the formation of drainage basins occurs over geologic time scales, while the distribution of vegetation reflects recent responses to climatic conditions. However, we note that changes in basin geomorphology can occur relatively fast in response to shifts in rainfall patterns [16], while vegetation communities may exhibit gradual and long-term responses to shifts in environmental conditions [9]. Thus, it is not clear that there exist characteristic spatial or temporal scales associated with the evolution of either geomorphological or ecological patterns. The increasing availability of continental-scale, high-resolution remotely sensed data regarding vegetation pattern should serve to reduce the disparity between the scales of ecological and geomorphological investigations. Such data will help in the development of a geographically and temporally broad understanding of the dynamic coupling between biological and hydrological processes in natural systems and river basins in particular.

### Acknowledgments

The Clayton Postdoctoral Fellowship at Princeton University and funding from the National Center for Earth-surface Dynamics (EAR-0120914) supported K.K. Caylor's research. S. Manfreda was supported by funds of the research program COS(OT). I.R.-I. acknowledges the support of NSF through the grants in Biocomplexity (DEB-0083566) and the National Center for Earth-surface Dynamics (EAR-0120914). We thank Shirley Kurc and Eric Small for assistance in developing vegetation and soil parameters.

### References

- [1] Albertson JD, Montaldo N. Temporal dynamics of soil moisture variability: I. Theoretical basis. *Water Resour Res* 2003;39(10):1274.
- [2] Bonan G. *Ecological climatology*. Cambridge: Cambridge University Press; 2003.
- [3] Brandes D, Wilcox BP. Evapotranspiration and soil moisture dynamics on a semiarid ponderosa pine hillslope. *J Am Water Resour Assoc* 2000;36(5):965–74.
- [4] Bridge SRJ, Johnson EA. Geomorphic principles of terrain organization and vegetation gradients. *J Vegetat Sci* 2000;11:57–70.
- [5] Caylor KK, Scanlon TM, Rodriguez-Iturbe I. Feasible optimality of vegetation patterns in river basins. *Geophys Res Lett* 2004;31(13):L13502.
- [6] Campbell GS, Norman JM. *An introduction to biophysics*. New York: Springer; 1998.
- [7] Clapp RB, Hornberger GM. Empirical equations for some soil hydraulic properties. *Water Resour Res* 1978;14(4):601–4.
- [8] Coughenour MB, Ellis JE. Landscape and climatic control of woody vegetation in a dry tropical ecosystem: Turkana district, Kenya. *J Biogeogr* 1993;20(4):383–98.
- [9] Delcourt PA, Delcourt HR. Long-term forest dynamics of the temperate zone: a case study of late-quaternary forests in eastern North America. New York: Springer-Verlag; 1987.
- [10] Friend AD. PGEN: an integrated model of leaf photosynthesis, transpiration, and conductance. *Ecol Modell* 1995;77:233–55.
- [11] Jones HG. *Plants and microclimate: a quantitative approach to environmental plant physiology*. Cambridge: Cambridge University Press; 1983.
- [12] Kim Y, Eltahir EAB. Role of topography in facilitating coexistence of trees and grasses within savannas. *Water Resour Res* 2004;40:W07505. doi: 10.1029/2003WR002578.
- [13] Laio F, Porporato A, Ridolfi L, Rodriguez-Iturbe L. Plants in water-controlled ecosystems: active role in hydrologic processes and response to water stress—II. Probabilistic soil moisture dynamics. *Adv Water Resour* 2001;24(7):707–23.
- [14] Laio F, Porporato A, Ridolfi L, Rodriguez-Iturbe I. Mean first passage times of processes driven by white shot noise. *Phys Rev E* 2001;63(3):#036105.
- [15] Larcher W. *Physiological plant ecology*. New York: Springer-Verlag; 1995.
- [16] Lavee H, Imeson AC, Sarah P. The impact of climate change on geomorphology and desertification along a Mediterranean-arid transect. *Land Degrad Dev* 1998;9(5):407–22.
- [17] Levin SA. The problem of pattern and scale in ecology. *Ecology* 1992;73(6):1943–67.
- [18] Marani M, Rigon R, Rinaldo A. A note on fractal channel networks. *Water Resour Res* 1991;27(12):3041–9.
- [19] Marani M, Rinaldo A, Rigon R, Rodriguez-Iturbe I. Geomorphological width functions and the random cascade. *Geophys Res Lett* 1994;21(19):2123–6.
- [20] Mohanty BP, Skaggs TH. Analysis and mapping of field-scale soil moisture variability using high-resolution ground-based data during the Southern Great Plains 1997 (SGP97) Hydrology Experiment. *Water Resour Res* 2000;36(4):1023–31.
- [21] Porporato A, Laio F, Ridolfi L, Rodriguez-Iturbe I. Plants in water-controlled ecosystems: active role in hydrological processes and response to water stress—III. Vegetation water stress. *Adv Water Resour* 2001;24(7):725–44.
- [22] Ridolfi L, D'Odorico P, Porporato A, Rodriguez-Iturbe I. Stochastic soil moisture dynamics along a hillslope. *J Hydrol* 2003;272(1–4):264–75.
- [23] Rietkerk M, Boerlijt MC, van Langvelde F, HilleRisLambers R, van de Koppel J, Kummur L, et al. Self-organization of vegetation in arid ecosystems. *Am Natur* 2002;160:524–30.
- [24] Rinaldo A, Rodriguez-Iturbe I, Rigon R, Ijjasz-Vasquez E, Bras RL. Self-organized fractal river networks. *Phys Rev Lett* 1993;70(6):822–5.
- [25] Rodriguez-Iturbe I, Rinaldo A, Rigon R, Bras RL, Ijjasz-Vasquez E. Energy dissipation, runoff production and the three-dimensional structure of channel networks. *Water Resour Res* 1992;28(4):1095–103.
- [26] Rodriguez-Iturbe I, Rinaldo A. *Fractal river basins: chance and self-organization*. New York: Cambridge University Press; 1997.
- [27] Rodriguez-Iturbe I, Porporato A, Ridolfi L, Isham V, Cox DR. Probabilistic modeling of water balance at a point: the role of climate, soil and vegetation. *Proc R Soc London: Ser A* 1999;455:3789–805.
- [28] Rodriguez-Iturbe I, Porporato A, Laio F, Ridolfi L. Plant strategies to cope with stochastic soil water availability. *Geophys Res Lett* 2001;28(2):4495–8.
- [29] Shore G. Height Statistics for Sevilleta LTER Vegetation Map. Sevilleta LTER Database, 1997. Available from: <<http://sevilleta.unm.edu/data/archive/plant/vegmap/classified/height/>> [08/2003].
- [30] Small E, Kurc S. Tight coupling between soil moisture and the surface radiation budget in semiarid environments: implications

- for land–atmosphere interactions. *Water Resour Res* 2003;39(10):1278–97.
- [31] Sole RV, Alonso D, McKane A. Self-organized instability in complex ecosystems. *Philos Trans R Soc London B* 2002;357:667–81.
- [32] Thierfelder TK, Grayson RB, von Rosen D, Western AW. Inferring the location of catchment characteristic soil moisture monitoring sites. Covariance structures in the temporal domain. *J Hydrol* 2003;280(1–4):13–32.
- [33] Turcotte DL. Implications of chaos, scale-invariance, and fractal statistics in geology. *Global Planetary Change* 1990;89:301–8.
- [34] Turcotte DL, Rundle JB. Self-organized complexity in the physical, biological, and social sciences. *Proc Nat Acad Sci USA* 2002;99:2463–5.
- [35] USDA Natural Resources Conservation Service. State Soil Geographic (STATSGO) Database, Miscellaneous Publication No. 1492, 1994.
- [36] Vogelmann JE, Howard SM, Yang L, Larson CR, Wylie BK, Van Driel N. Completion of the 1990s national land cover data set for the conterminous United States from Landsat Thematic Mapper data and ancillary data sources. *Photogramm Eng Remote Sens* 2001;67:650–2.
- [37] Wilcox BP, Breshears DD, Allen CD. Ecohydrology of a resource-conserving semiarid woodland: Effects of scale and disturbance. *Ecol Monogr* 2003;73(2):223–39.
- [38] Wilcox BP. Runoff and erosion in intercanopy zones of pinyon–juniper woodlands. *J Range Manage* 1994;47(4):285–95.
- [39] Williams DG, Ehleringer JR. Intra- and interspecific variation for summer precipitation use in pinyon–juniper woodlands. *Ecol Monogr* 2000;70(4):517–37.
- [40] Yan S, Wan C, Sosebee RE, Wester DB, Fish EB, Zartman RE. Responses of photosynthesis and water relations to rainfall in the desert shrub creosote bush (*Larrea tridentate*) as influenced by municipal biosolids. *J Arid Environ* 2000;46:397–412.
- [41] Yang Y, Milne B. Water balance modeling project vegetation plots data, Sevilleta LTER database, 1997. Available from: <<http://sevilleta.unm.edu/data/contents/SEV081/>> [1 August 2003].